Source of Radio Emissions Induced by the Galilean Moons Io, Europa and Ganymede: In Situ Measurements by Juno

C K Louis, P. Louarn, B. Collet, S. Al Saati, J R Szalay, V. Hue, L. Lamy, S. Kotsiaros, W S Kurth, C M Jackman, et al.

Source of radio emissions induced by the Galilean moons Io, Europa and Ganymede: *in situ* measurements by Juno

C. K. Louis[1,2,3], P. Louarn[2], B. Collet[4], N. Clément[2,5], S. Al Saati[2,6], J. R. Szalay[7], V. Hue[8], L. Lamy[3,4], S. Kotsiaros[9], W. S. Kurth[10], C. M. Jackman[1],Y. Wang[2,11,12], M. Blanc[2,5], F. Allegrini[13,14], J. E. P. Connerney[15], D. Gershman[16]

[1]School of Cosmic Physics, DIAS Dunsink Observatory, Dublin Institute for Advanced Studies, Dublin 15, Ireland
[2]IRAP, Université de Toulouse, CNRS, CNES, UPS, Toulouse, France
[3]LESIA, Observatoire de Paris, Université PSL, CNRS, Sorbonne Université, Université de Paris, Meudon, France
[4]Aix Marseille Université, CNRS, CNES, LAM, Marseille, France
[5]Laboratoire d'Astrophysique de Bordeaux, Univ. Bordeaux, CNRS, B18N, Allée Geoffroy Saint–Hilaire, 33615 Pessac, France
[6]CPHT, CNRS, Institut Polytechnique de Paris, Route de Saclay, 91128 Palaiseau, France
[7]Department of Astrophysical Sciences, Princeton University, Princeton, New Jersey, USA
[8]Aix–Marseille Université, CNRS, CNES, Institut Origines, LAM, Marseille, France
[9]Technical University of Denmark: Kgs. Lyngby, Denmark
[10]Department of Physics and Astronomy, University of Iowa, Iowa City, Iowa, USA
[11]State Key Laboratory of Space Weather, National Space Science Center, Chinese Academy of Sciences, Beijing, China.
[12]College of Earth and Planetary Sciences, University of Chinese Academy of Sciences, Beijing, China.
[13]Southwest Research Institute, San Antonio, Texas, USA
[14]Department of Physics and Astronomy, University of Texas at San Antonio, San Antonio, Texas, USA
[15]Space Research Corporation, Annapolis, MD, USA 21403
[16]NASA Goddard Space Flight Center, Greenbelt, MD, USA

Key Points:

- All Jupiter–moon radio emissions are shown to be similarly triggered by the CMI.
- The crossed radio sources are colocated with either MAW, RAW or TEB footprints.
- The crossed radio sources coincide with downward field–aligned currents and Alfvén perturbations.

Corresponding author: C. K. Louis, `corentin.louis@obspm.fr`

Abstract

At Jupiter, part of the auroral radio emissions are induced by the Galilean moons Io, Europa and Ganymede. Until now, except for Ganymede, they have been only remotely detected, using ground–based radio–telescopes or electric antennas aboard spacecraft. The polar trajectory of the Juno orbiter allows the spacecraft to cross the range of magnetic flux tubes which sustain the various Jupiter–satellite interactions, and in turn to sample *in situ* the associated radio emission regions. In this study, we focus on the detection and the characterization of radio sources associated with Io, Europa and Ganymede. Using electric wave measurements or radio observations (Juno/Waves), *in situ* electron measurements (Juno/JADE–E), and magnetic field measurements (Juno/MAG) we demonstrate that the Cyclotron Maser Instability (CMI) driven by a loss–cone electron distribution function is responsible for the encountered radio sources. We confirmed that radio emissions are associated with Main (MAW) or Reflected Alfvén Wing (RAW), but also show that for Europa and Ganymede, induced radio emissions are associated with Transhemispheric Electron Beam (TEB). For each traversed radio source, we determine the latitudinal extension, the CMI–resonant electron energy, and the bandwidth of the emission. We show that the presence of Alfvén perturbations and downward field–aligned currents are necessary for the radio emissions to be amplified.

Plain Language Summary

At Jupiter, the auroras are much more intense and long-lasting than on Earth, and some are influenced by Jupiter's three largest moons: Io, Europa, and Ganymede. We're particularly interested in the radio signals from these auroras. Until recently, these signals were mainly studied from a distance, using Earth-based telescopes or spacecraft passing by Jupiter. However, since 2016, the Juno spacecraft has been orbiting Jupiter, flying through the auroral zone. Our study investigates the creation of these radio auroras using Juno's instruments to measure radio waves, particles, and magnetic fields. Our research strongly suggests that a phenomenon called the Cyclotron Maser Instability is the cause of these radio signals. This instability happens because some electrons are not coming back from Jupiter after causing Ultraviolet aurora on top of Jupiter's atmosphere. These radio signals are connected to the moons' ultraviolet auroras. Additionally, our research highlights the importance of specific perturbations in Jupiter's magnetic field, known as Alfvén perturbations, and currents that link Jupiter to these moons. This study deepens our understanding of Jupiter-moon interactions and sheds light on Jupiter's fascinating auroras.

1 Introduction

One of the main objectives of the Juno mission is to probe Jupiter's auroral regions *in situ* (Bagenal et al., 2017) and, in particular, to search for the sources of auroral radio emission. This is made possible by a suite of instruments capable of acquiring high–quality plasma and wave measurements, such as Waves (Kurth et al., 2017), JADE–E (Jovian Auroral Distributions Experiment–Electrons, McComas et al., 2017) and MAG (Connerney et al., 2017). Imagers on–board Juno are also really useful to compare with auroral emissions in other wavelengths, such as in ultraviolet with the UVS instrument (Ultraviolet Spectrograph Gladstone et al., 2017).

These instruments provide measurements to study the radio wave amplification process, and have already been able to locate the position of the sources (Imai et al., 2017, 2019; Louis et al., 2019a) and to confirm the Cyclotron Maser Instability (CMI) as their underlying generation mechanism (Louarn et al., 2017, 2018; Louis et al., 2017a, 2020; Collet et al., 2023, and see below for more details).

The Galilean moons Io, Europa and Ganymede are known to induce auroral emissions, at radio (Bigg, 1964; Louis et al., 2017b; Zarka et al., 2017, 2018; Jácome et al., 2022), ultraviolet (UV, Prangé et al., 1996; Clarke, 1998; Clarke et al., 2002) and infrared (Connerney et al., 1993; Mura et al., 2017, 2018) wavelenghts . The motion of the moons across Jupiter's magnetosphere in the plasma torus surrounding them (Szalay et al., 2022) generates an electric field, inducing electric currents and/or Alfvén waves (Goldreich & Lynden-Bell, 1969; Neubauer, 1980; Saur, 2004) which both accelerate electrons along the magnetic field lines in the moons' flux tubes to kilo–electron–volts (keV) energy. Note that the case of Callisto is not studied here, even if a tentative detection of the Callisto UV footprint has been reported (Bhattacharyya et al., 2018), and hints of radio emissions have been observed to this day using Galileo and Voyager data (Menietti et al., 2001; Higgins, 2007). To date, Juno has not observed any UV or radio emissions likely to be induced by Callisto, nor any intensification of the electron energy flux while crossing Callisto's flux tubes..

The Io, Europa, and Ganymede induced UV emissions are known to be produced by downgoing electrons interacting with the Jovian neutral atmosphere. These signatures are observed at the moons' magnetic footprint and along their tails, i.e the longitudinal extension of these spots in the downstream direction relative to the plasma flow encountering the moon (Bonfond et al., 2017a, 2017b). Recent *in situ* studies probed the magnetic field lines connected to these UV footprints, and found that they are consistent with production by Alfvénic interaction (Szalay et al., 2018, 2020a, 2020b; Allegrini et al., 2020). On the radio side, the moons' induced emissions are believed to be produced by the CMI and have already been simulated and well match the observations (Hess et al., 2008; Louis et al., 2017a, 2019b). This mechanism is also responsible for the auroral radio emission (independent of the moons) and has been verified *in situ* by Louarn et al. (2017, involving loss–cone electron distribution functions, or EDF), Louarn et al. (2018, conics–type EDF) and Collet et al. (2023, shell–type EDF). Recently, Louis et al. (2020) showed with *in situ* Juno measurements that the radio emission induced by the Jupiter–Ganymede interaction is indeed produced by the CMI, from a loss cone–type EDF, i.e., a lack in the up–going electron population, with a characteristic energy of 4–15 keV.

Since Jupiter–satellite radio and UV emissions are expected/assumed to be colocated (Hess et al., 2010), the question of the link between these emissions at two different wavelengths naturally arises. In the Io case, we know that UV and radio auroral emissions are produced by Alfvénic interactions, and that the main and secondary radio emissions are respectively produced on the magnetic field lines connected to the main Alfvén wing (MAW) and reflected Alfvén wing (RAW) spots, and highly suspected for the Transhemispheric Electron Beam (TEB) spots (Hess et al., 2010; Lamy et al., 2022). But no simultaneous *in situ* measurements have yet been analyzed. In the Ganymede case, Louis et al. (2020) showed, extending the work of Szalay et al. (2020a), that radio emission is produced above a magnetic flux tube mapping to a UV RAW spot. Hue et al. (2022) showed that radio emission seems to be produced above the TEB spot. Finally in the Europa case, UV emissions have been observed at the moon's footprint and along the moon's footprint tail (Bonfond et al., 2017a, 2017b; Allegrini et al., 2020; Hue et al., 2023; Rabia et al., 2023), but no simultaneous observation of UV and radio emissions has yet been analyzed.

This study is a follow–up of the Louis et al. (2020) analysis, focusing on the three known types of Jupiter–satellite radio emissions. In Section 2, we briefly recall the theory of the Cyclotron Maser Instability. In Section 3, we present the observations of Jupiter–Io (J–I), –Europa (J–E) and –Ganymede (J–G) radio emission source crossings and calculate the CMI growth rate (whenever possible) and determine the emission parameters. Finally, in Section 4, we summarize and discuss the results.

2 The Cyclotron Maser Instability

The CMI is known to be responsible for the production of auroral radio emission of Earth, Saturn and Jupiter (Wu & Lee, 1979; Le Queau et al., 1984a, 1984b; Wu, 1985; Pritchett, 1986; Treumann, 2006; Mutel et al., 2010; Lamy et al., 2010; Kurth et al., 2011; Louarn et al., 2017, 2018).

In a tenuous and sufficiently magnetized plasma, i.e., wherever the electron plasma frequency f_{pe} is much lower than the electron cyclotron frequency f_{ce}, and with weakly out–of–equilibrium/non–maxwellian relativistic electrons, the CMI can directly amplify X–mode waves at a frequency close to the electron cyclotron frequency f_{ce}. The radio waves are then emitted at a certain beaming angle θ from the local magnetic field B ($k\cos\theta = \vec{k}\cdot\vec{B} = k_{||}$ the parallel component of the wave vector $\mathbf{k}$), which by symmetry around the local magnetic field line forms a hollow cone of emission. The CMI is a wave–electron instability for which the resonance condition is reached when the Doppler–shifted angular frequency of the wave in the frame of the electrons ($\omega - k_{||}v_{r_{||}}$) is equal to the relativistic gyration frequency of resonant electrons ($\omega_{ce}\Gamma_r^{-1}$):

$$\omega = \omega_{ce}\Gamma_r^{-1} + k_{||}v_{r_{||}} \quad , \tag{1}$$

with $\mathbf{k}$ the wave vector and v_r the velocity of the resonant particle, and $\Gamma_r^{-1} = \sqrt{1 - v_r^2/c^2}$ the relativistic Lorentz factor. The $_\perp$ and $_{||}$ indices represent the perpendicular and parallel components of the wave vector $\mathbf{k}$ or the velocity v_r with respect to the magnetic field B.

In the weakly relativistic case ($v_r \ll c$), the above resonance condition can be rewritten as the equation for a resonant circle in the $[v_\perp, v_{||}]$ velocity space:

$$v_\perp^2 + (v_{||} - v_0)^2 = v_r^2 \quad , \tag{2}$$

defined by its center:

$$v_0 = \frac{k_{||}c^2}{\omega_{ce}} \quad , \tag{3}$$

and its radius

$$v_r = \sqrt{v_0^2 - 2c^2\Delta\omega} \quad , \tag{4}$$

with

$$\Delta\omega = (\omega - \omega_{ce})/\omega_{ce} \tag{5}$$

the frequency shift between the emission frequency and the cyclotron electron frequency.

For the CMI to amplify radio emissions, the wave growth rate calculated along this resonance circle must be positive. The simplified version of the growth rate expression used by Louarn et al. (2017, 2018) and Louis et al. (2020) is well adapted to the amplification of X–mode waves propagating at frequencies close to f_{ce}, for a refraction index $N = 1$ and a moderately energetic ($E \ll 511$ keV) and low–density ($f_{pe} \ll f_{ce}$) plasma. But this expression contains an approximation at low pitch angle, and therefore applies only to growth rate calculation in the loss cone. Therefore to generalize the calculation of growth rate in the whole electron distribution function, we use the expression of Collet et al. (2023), derived from the dispersion relation in X mode from Le Queau et al. (1984b) (see Annexe A of Collet et al., 2023, for the full demonstration of the growth rate expression). They assumed that the plasma is composed of one cold population at thermodynamic equilibrium that support wave propagation and one non–thermal energetic (or hot) population that feeds the instability.

$$\gamma = \frac{(\frac{\pi}{2}\epsilon_h)^2}{1+(\frac{\epsilon_c}{2\Delta\omega})^2} c^2 \int_0^\pi d\phi \; v_r^2 \sin^2(\phi) \frac{\partial f_h}{\partial v_\perp}(v_0 + v_r\cos(\phi), v_r\sin(\phi)) \tag{6}$$

In this equation $\epsilon_\alpha = \omega_{p\alpha}/\omega_{ce}$, where $\omega_{p\alpha}$ is the plasma frequency of the hot ($\alpha =$ h) or cold ($\alpha =$ c) electrons. f_h is the normalized electron distribution function of hot electrons ($\int f_h dv^3 = 1$). In practice, the factor to normalize the distribution function is $c^3 10^{-18}/n_e$, where n_e is the electron density (in cm^{-3}). In this study, the hot electron density is the one measured by JADE–E for electrons above 1 keV energy (as in Collet et al., 2023). Note that, in the examples presented in Section 3, the mean ratio between hot and cold population is $n_{\text{hot}}/n_{\text{total}} = 0.3$.

Equation 6 means that the growth rate is obtained by integrating $\partial f_h/\partial v_\perp$ along a resonant circle in the normalized velocity space [$v_{||}$,$v_\perp$], defined by its center v_0 (Equation 3), its radius v_r (Equation 4) and the angle $\phi \subseteq$[0–π] along this circle.

By calculating and maximizing the growth rate, we are able to assess the most CMI–unstable electron population and characterize the resulting amplified waves, and then obtain the characteristics of the emission (e.g., the energy of the resonant electrons and the aperture of the beaming angle).

One of the 3 anodes of JADE–E is unfortunately not functional. As a result, due to Juno's spin and its orientation with respect to the magnetic field lines, some pitch angles may not be sampled (up to one third of the electron distribution function). In order to calculate the growth rate of the wave along the different resonance circles in velocity space, JADE–E needs to sample sufficient pitch angles. If too much of the EDF measurement is missing (60% along a resonant circle), we cannot calculate the growth rate and determine the characteristics.

However, assuming that Juno is located within the radio source region (if the radio emission is observed very close to, or even below, f_{ce}), we are still able to obtain some information about the source size and the characteristics of the emission, by measuring the emission frequency observed by Juno/Waves data. If the EDF is of shell type, i.e. if $f \leq f_{\text{ce}}$, then the resonant circle is centered on $v_0 = 0$, therefore $k_{||} = 0$ (see Equation 3), and Equation 1 can then be rewritten as:

$$\omega_{shell} = \omega_{ce}\sqrt{1-\frac{v_r^2}{c^2}} \quad . \tag{7}$$

Thus, from the measurements of the local electron cyclotron frequency ($\omega_{ce} = 2\pi f_{ce}$) and the emission frequency f_{shell}, and using $E = 0.5 \times m_e v^2$ (with $m_e = 511$ keV/c^2 the electron mass), the electron energy in keV in the shell–driven CMI case can be written as:

$$E = 255.5 \times \left(1 - \left(\frac{f_{\text{shell}}}{f_{\text{ce}}}\right)^2\right) \quad . \tag{8}$$

In the case of a loss–cone (lc) type EDF, i.e. if $f > f_{\text{ce}}$, the resonant equation can be rewritten as (for more details see Equations 2–12 of Louis et al., 2019b):

$$\omega_{lc} = \frac{\omega_{ce}}{\sqrt{1-\frac{v_r^2}{c^2}}} \quad , \tag{9}$$

and therefore the electron energy in keV in the loss cone–driven CMI case can be written as:

$$E = 255.5 \times \left(1 - \left(\frac{f_{ce}}{f_{\rm lc}}\right)^2\right) \quad (10)$$

3 Observations and Analysis of Radio Emission Sources Crossings

Due to the large extension of Io's tail (Szalay et al., 2020b) and to Juno's polar orbit, the spacecraft crossed Io's magnetic flux tubes at least twice every orbit (North, then South). However, electron fluxes connected to Io's UV aurora are not observed in appreciable or detectable amounts by Juno/JADE–E every transit of these flux tubes. Therefore, during the first 26 Juno perijoves, 18 cases of electron fluxes connected to Io's magnetic flux tube have been reported using the JADE–E measurements (Szalay et al., 2020b). By studying the data from perijoves (PJ) #27 to #31, we report five more cases of Io's tail flux tube crossing where electron fluxes were measured. In the Europa case, electron fluxes connected to Europa's UV aurora were measured ten times (Allegrini et al., 2020; Rabia et al., 2023). Finally, electron flux connected to Ganymede's UV aurora were measured only two times. The first one during PJ #20 (reported by Szalay et al., 2020a; Louis et al., 2020) and the second one during PJ #30 (studied in details by Hue et al., 2022).

For all moon's flux tube crossings detected by JADE–E, we investigate Waves observations to look for radio emission located below 1 % the local electron cyclotron frequency $f_{\rm ce}$ (determined from the local magnetic field amplitude measured by the MAG instrument). We therefore considered these cases as a potential crossing of a radio source. We then study the EDF obtained from JADE–E. Szalay et al. (2020a, 2020b); Allegrini et al. (2020); Rabia et al. (2023) studied the downward electrons and the production of UV emissions linked to these downward electron currents, as well as the presence of Alfvénic current systems capable of accelerating these electrons. We study here the CMI–unstability of measured EDF, in the continuity of Louis et al. (2020). To go further than Louis et al. (2020), we study instability in the whole EDF, to search not only for loss–cone type instabilities, but also shell type. We also study the upward and downward electrons, as well as the magnetic field perturbation, to determine the presence of field–aligned currents (FAC) using Wang et al. (2021) and Al Saati et al. (2022) method and Alfvén perturbations capable of accelerating electrons.

Downtail distances with respect to the main spot were recently revised using Juno/UVS data. Over 1,600 spectral images of the Io, Europa, and Ganymede UV footprint were analyzed to provide statistical positions of the main Alfvén wing spots. This allowed Hue et al. (2023) to estimate the distance from Juno to the main spot at the time of the source crossings that will be described in this Section, as well as derived observationally an estimation of the Alfvén travel time for each three moons. Note that the actual position of the main Alfvén wing spots is affected by the background magnetospheric conditions (density of the plasma sheet along the field line connected to the satellite footprint and/or magnetic field strength), and therefore shifts of the main Alfvén wing spots mapped to the equatorial region up to $\pm 2^o$ (Io), $\pm 4^o$ (Europa) and $\pm 5^o$ (Ganymede) are not unusual (See Hue et al., 2023, Figures 4, 5, 7). A negative distance to the main spot therefore translate either (i) a source crossing associated with a transhemispheric electron beam located much upstream of the Alfvén wing spots, or (ii) a change in the plasma condition (e.g., lower plasmasheet density and/or higher magnetic field magnitude).

3.1 Jupiter–Io radio emission source crossings

Out of the 23 cases where electron fluxes connected to Io's tail flux tube were measured, simultaneous radio emissions below $1.01 \times f_{\rm ce}$ were observed in only 4 cases. Figure 1 displays Juno measurements around an Io flux tube encounter, during PJ#5 on 2017–03–27 (2017 March 27th) in the Southern hemisphere (already reported by Louis et al., 2019a). Panel (A) presents the Juno/Waves measurements (in low–resolution mode, Kurth et al., 2017) around the perijove (from ~ -1.5 h before to ~ 2.5 h after). Panel (B) is a 5 min zoom–in of panel (A) using Juno/Waves high–resolution mode. The decreasing solid–black and dashed–black lines in panels (A,B) represent respectively the electron cyclotron frequency f_{ce} and $1.01\times f_{ce}$. Panels (C)–(E) show the Juno/JADE–E measurements of (C) the electron differential number flux (or intensity), (D) the electron distribution function of upgoing electrons and (E) the partial electron density (where all the energy population < 0.1 keV is not accounted for). Figure 1F displays the FAC calculated based on Al Saati et al. (2022)'s method (see sections 1.3 and 2 of their SI for more details). This method used the residual magnetic field perturbation δB, defined as the difference between the Juno/MAG magnetic field measurements and the magnetic field values obtain from the combination of the Connerney et al. (2018) magnetic field and Connerney et al. (1981) current sheet models. The FAC are then calculated from the residual magnetic field perturbation in the azimuthal direction (δB_ϕ).

Figure 1B displays an emission very close to $1.01 \times f_{ce}$, while we observe an enhancement in the electron energy flux (panel C) at a few keV, a strong intensification in the distribution function (panel D), an increase of the electron density (panel F) and a clear upward current surrounded by downward FAC (panel G). Figure S1 in Supporting Information displays the magnetic field fluctuations for all the magnetic field components in spherical coordinates. The magnetic field perturbation associated to the FAC shows clear fluctuations in the transverse component (perpendicular to B, corresponding to δB_ϕ and δB_θ) while no fluctuations are observed in the radial component (δB_r). The fluctuations are therefore confined to the transverse components, which is indicative of a lack of horizontal current, and therefore indicative of FAC (displayed Figure 1G). Moreover, no fluctuations are seen in the total magnetic field magnitude $\delta|B|$, indicating that these variations are Alfvénic in nature (Gershman et al., 2019; Kotsiaros et al., 2019).

Figures 2A–B display the electron distribution function in the velocity space measured by Juno/JADE–E at (A) 09:30:52 and (B) 09:31:00. From these data and Equation 6 we can calculate the normalized growth rate of the emission along different resonant circles to determine the unstable electron population. Figures 2C–D show the estimated normalized growth rate γ/ω_{ce} along resonant circles in the whole EDF, calculated for different centers (x–axis) and different radii (y–axis). Figures 2E–F displays the growth rate γ as a function $\Delta\omega$ for each resonant circle displaying a positive growth rate.

Positive growth rates are obtained for the EDF of Figure 2A, and not for the EDF of Figure 2B. Only resonant circles inside the theoretical loss cone show positive growth rate (blue circles and orange stars in Figure 2E), while no positive growth rate are found for shell–type resonant circles (green diamonds). By doing this calculation before, during and after the crossing of the Io's tail flux tube (see Figure 1E), we are able to determine when Juno is in the source, and thus determine its size and the characteristics of the emission. In this case, positive growth rate are obtained along loss–cone type resonant circles from 09:30:51 to 09:30:59 ($\pm$1 sec). This time interval is indicated in Figure 1 by the two vertical dashed red lines. Juno's velocity being ~ 45 km/s during this time, we determined that the source size is 360 ± 45 km. From the growth rate calculation, we can determine that the energy of the resonant electrons responsible for this emission is in the range [1–15] keV, with an opening angle θ of the beaming cone in the range [74°–85°]. To determine this value, we used Equation 7 of Louis et al. (2020):

$$\theta = \mathrm{acos}(\beta_0/(1+\Delta\omega)) \quad , \tag{11}$$

based on the assumptions of Section 2.

It is interesting to note that enhanced electron fluxes are observed for the period of 09:30:51 to 09:31:02 (determined as the flux tube crossing, Szalay et al., 2020b), while the J–I radio source is only crossed from 09:30:51 to 09:30:59 (determined from the growth

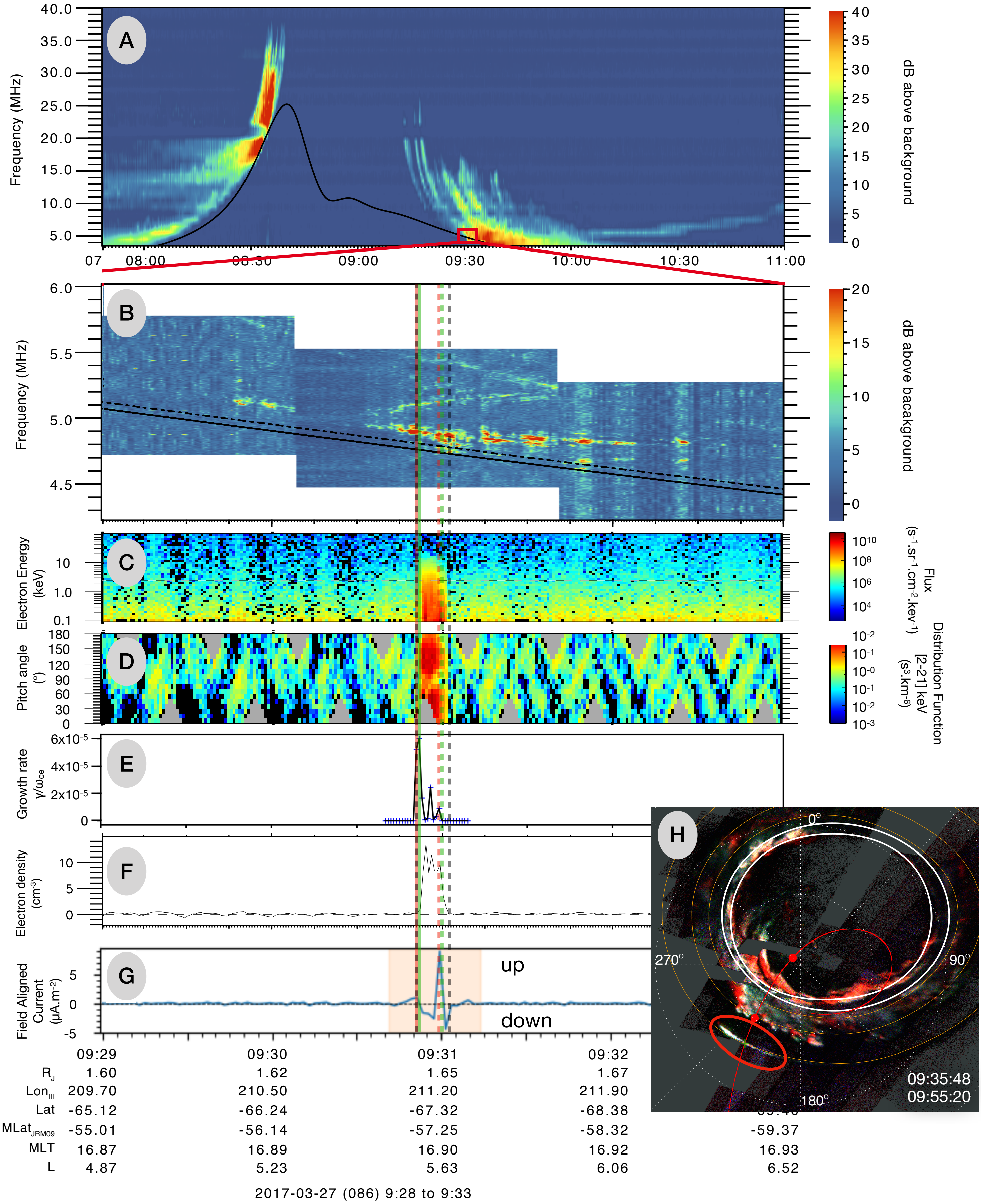

Figure 1: Caption on next page

Figure 1: Juno data during Perijove 5, on 27 March 2017. Panels (A,B) display Juno/Waves data (A) in low–resolution mode and (B) in high–resolution mode. The solid–black lines represent the electron cyclotron frequency derived from the magnetic field measurements of Juno/MAG, and the dashed–black line is $1.01 \times f_{\text{ce}}$.Panels (C–D) display Juno/JADE–E measurements: (C) the electron differential number flux (or intensity) of all electrons; (D) the electron distribution function for energy in range [2–21] keV as a function of pitch angles; Panels (E) displays the normalized growth rate $\gamma/\omega_{\text{ce}}$ maximal value calculated using Equation 6. Panel (F) shows the partial electron density calculated from the JADE–E flux. Panel (G) shows the field–aligned currents calculated based on Al Saati et al. (2022)'s method, using magnetic field fluctuations in the azimuthal direction (δB_ϕ) deduced from the Juno/MAG measurements.The vertical dashed black lines represent the flux tube crossing as inferred from JADE data, while vertical dashed red lines represent the time interval where positive growth rate are calculated from JADE–E measurements. The vertical solid and dashed green lines indicate where the electron distribution functions displayed in Figure 2 are taken. Panel (H) displays a UV map of the southern hemisphere, using Juno/UVS measurements from 09:35:49 to 09:55:20. The red line indicates Juno's trajectory, with the red dots its position at the start and end time of the measurements used for this image. Io UV footprint is highlighted by the red ellipse.

rate calculation), which corresponds to the time where Juno is inside a downward current (corresponding to upward electrons). When Juno is located inside an upward current (i.e., downward electrons), no positive growth rate are obtained.

The same method is applied to the data from PJ#6 (North) on 2017–05–19, during which a J–I radio source is crossed between 05:39:31 and 05:39:39 (see Figure S2), and to PJ#29 (North) on 2020–09–16 during which a J–I radio source is crossed between 02:00:34 and 02:00:36 (see Figure S3). For the crossing of the J–I radio source that occurs in the northern hemisphere during PJ#5 on 2017–03–26 around 08:34:40 (see Figure S4), we do not have JADE–E measurements of the upgoing electrons, and we therefore can not calculate the growth rate. Since no radio emission is observed below f_{ce}, we therefore assume that loss–cone EDF remain the prominent source of free energy for the CMI, and we therefore use Equation 10 to determine the electron energy. The results for these three crossings, i.e., radio source size, resonant electron energy, $\text{f}_{\text{emission}}$ and opening angle of the beaming cone, are summarized Table 1.

As for PJ#5 (South), FAC and Alfvénic perturbations are observed during PJ#5 (North) and PJ#29 (North) Io's flux tube crossing (see Figures S4 and S3, respectively), with perturbations in the transverse components of the magnetic field (δB_ϕ and δB_θ) while no perturbation is observed in the radial (δB_r) and compressive ($\delta|B|$) components. Furthermore, as for PJ#5 (South), the radio source is not crossed anywhere inside Io's flux tube, but only when Juno is located inside a downward current (i.e., upward electrons). During PJ#6 (North), nothing is observed in the magnetic field perturbations, which could be due to the fact that the electron density is very low (< 1 cm^{-1}), which could induce a perturbation too weak for the MAG instrument to detect.

Based on the recalculation of the downtail distance to the main spot of Io $\Delta\lambda_{\text{Alfvén}}$ (Hue et al., 2023), the J–I radio emission source crossings of PJ#5 North, PJ#5 South, PJ#6 South are all associated with a Reflected Aflvén Wing (RAW) spot downtail of Io. The intensity of the radio emission seems to be quite similar for crossings occurring close to the main spot, with an intensity of 2–3$\times10^{-6}$ V^2.m^{-2}.Hz^{-1} when $3.3^{\text{o}} < \Delta\lambda_{\text{Alfvén}} < 10.8^{\text{o}}$. The intensity seems to be lower when $\Delta\lambda_{\text{Alfvén}}$ is large, with an intensity of 8×10^{-8} V^2.m^{-2}.Hz^{-1} for $\Delta\lambda_{\text{Alfvén}} = 87.4^{\text{o}}$.

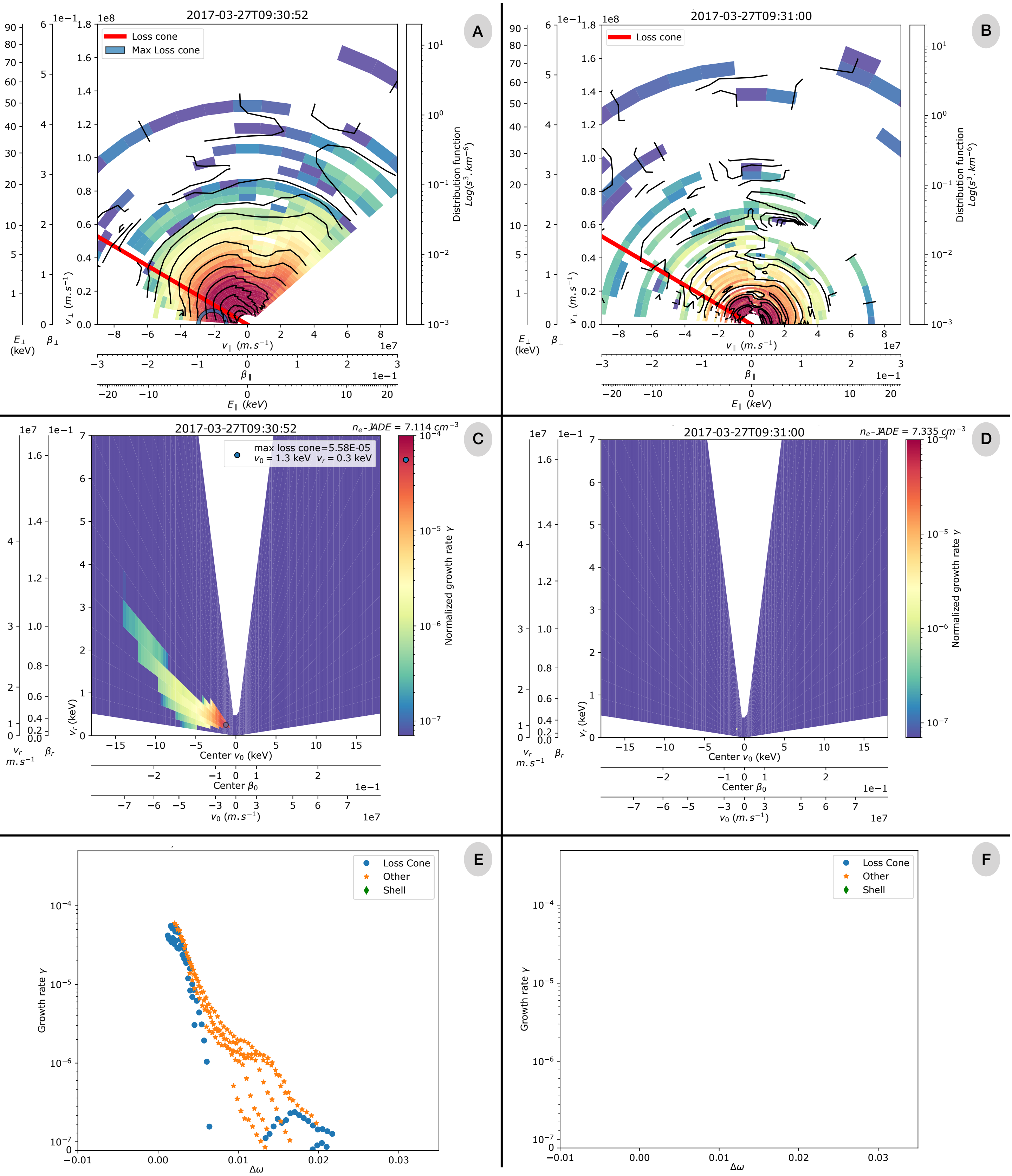

Figure 2: Caption on next page

Figure 2: Panels (A,B): electron distribution function in the velocity space $[v_{||}, v_{\perp}]$ measured by JADE–E on 2017–03–27 at (A) 09:30:52 (inside the Io tail radio source, see vertical solid green line Figure 1) and (B) 09:31:00 (outside the Io tail radio source, but inside Io's flux tube, see vertical dashed green line Figure 1). In that case, the $v_{||} < 0$ part of the EDF represents upgoing electrons, while $v_{||} > 0$ represents downward electrons. The colorbar and the isocontours are shown using a logarithmic scale in units of $s^3.km^{-6}$. The radial red thick line indicates the theoretical loss cone value. The blue circular half–circle in panel (A) display the resonant circle with the highest growth rate. Panels (C,D): Normalized growth rate (γ/ω_{ce}) estimates for different resonant circles at different centers v_0 and radii v_r. Panels (E,F): Normalized growth rate as a function of the frequency shift $\Delta\omega$ between the emission frequency and the cyclotron electron frequency (see Equation 5 for all resonant circle with positive growth rate γ. Blue circles represent growth rate for resonant circles tangential to the theoretical value of the loss cone. Orange stars represent growth rate growth rate for resonant circle inside the theoretical loss cone. Both are considered as loss–cone type instabilities. Green diamonds represent growth rate for resonant circles of shell-type.

3.2 Jupiter–Europa radio emission

During the 26 first perijoves, enhanced electron fluxes connected to Europa's UV aurora were measured ten times (Allegrini et al., 2020; Rabia et al., 2023). A radio source was crossed only during PJ#12 on the Northern hemisphere, on 2018–04–01 around 08:15:44.

Figure 3 displays Juno/Waves (panels A–B), Juno/JADE–E measurements (panels C–E) and Juno/UVS (panel F) during the crossing of flux tube connected to a Europa's downtail UV footprint (Allegrini et al., 2020). During the time of the flux tube crossing, determined by the enhancement of the electron flux in JADE–E measurements (Figures 3C–D), a radio emission is observed below $1.01 \times f_{ce}$ (Figure 3B). However, the JADE–E instruments did not record data of upgoing electrons in the loss cone during this time. We therefore cannot calculate the loss–cone or shell CMI growth rate for this EDF. Since no radio emission is observed below f_{ce}, we therefore assume that loss–cone EDF remain the prominent source of free energy for the CMI. We then apply Equation 10 to estimate the energy of the resonant electron. Looking at the Juno/Waves measurements (Figure 3B), we determine that the radio emission observed during Europa's flux tube crossing is emitted at a frequency between 0.7 and 1.5% above the electron cyclotron frequency f_{ce} (solid dark line). This frequency measurement leads to an energy of the resonant electrons in the range [3–8] keV, and an opening angle of the beaming cone in the range [79°–84°].

The MAG measurements of the magnetic field perturbation show no strong variation of the different components. Once again, as in the case of PJ#6N for Io, the electron density is very low (~ 2 cm^{-1}) which could induce perturbations too weak and/or too short for the MAG instrument to detect.

Based on the latest work of Rabia et al. (2023) and the recalculation of $\Delta\lambda_{\mathrm{Alfvén}}$ (Hue et al., 2023), we can conclude that the J–E radio source crossed during PJ#12 is associated with a Transhemispheric Electron Beam (TEB) spot uptail of the main Europa UV spot.

3.3 Jupiter–Ganymede radio emission

So far, flux tubes connected to Ganymede footprint tail aurora have been crossed twice: the first one during PJ #20 on 2019–05–19 between 07:37:14 and 07:37:32 (reported

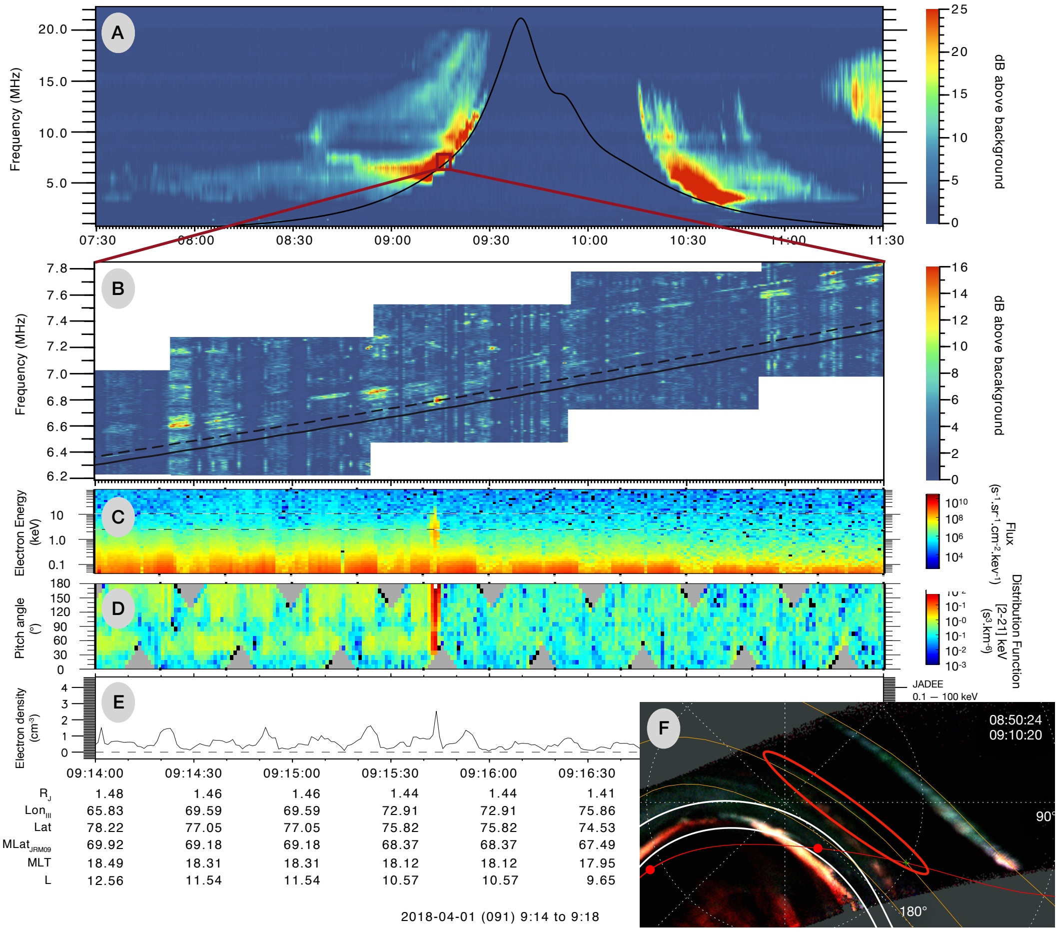

Figure 3: Panels (A,B) display Juno/Waves data (A) in low–resolution mode and (B) in high–resolution mode. The solid–black lines represent the electron cyclotron frequency derived from the magnetic field measurements of Juno/MAG, and the dashed–black line is 1.01 $\times$ f_{ce}. Panels (C–E) display Juno/JADE–E measurements: (C) the electron differential number flux (or intensity) of all electrons; (D) the electron distribution function for energy in range [2–21] keV only for pitch angles [0°–60°] corresponding to up–going electrons; (E) partial electron density calculated from the JADE–E flux. Panel (F) displays a UV map of the northern hemisphere, using Juno/UVS measurements from 08:50:24 to 09:10:20. The red line indicates Juno's trajectory, with the red dots its position at the start and end time of the measurements used for this image. Europa UV footprint is highlighted by the red ellipse.

by Szalay et al., 2020a; Louis et al., 2020) and the second one during PJ #30, on 2020–11–08 around 02:55:02 (Hue et al., 2022).

We already reported the PJ#20N crossing in Louis et al. (2020), but at that time, we did not look at the Juno/MAG measurements, which was done by Szalay et al. (2020a) (and plotted in Figure S5). During this Ganymede footprint tail aurora flux tube crossing, fluctuations in the transverse components (δB_ϕ and δB_θ) were observed, while no fluctuations were measured in the radial (δB_r) and compressive ($\delta|B|$) components, which indicates the presence of field–aligned currents and Alfvénic perturbations. As for the J–I radio emission sources, it should be noted that the radio source is only crossed when Juno is in a downward current (i.e., upward electrons). Based on Szalay et al. (2020a); Louis et al. (2020), this radio emissions is associated with a RAW UV spot (with a $\Delta\lambda_{\text{Alfvén}} = 8°$). However, based on the recent work of Hue et al. (2023), for this J–G radio source, $\Delta\lambda_{\text{Alfvén}} = -1.8°$. Therefore, due to the error of $\pm 5°$ on the position of the MAW for Ganymede (due to possible change in the *in situ* plasma condition, see penultimate paragraph of Section 1), it appears that the J–G radio source crossed during PJ#20, is connected not to the RAW spot, but to the MAW spot.

Concerning the second case, during PJ#30 on 2020–11–08 (northern hemisphere), Ganymede footprint tail aurora flux tube was crossed around 02:55:02, with radio emission tangent to $1.01 \times f_{ce}$ at the same time (see Hue et al., 2022). Unfortunately, the field–of–view of JADE–E was unable to measure the upward electrons during Ganymede flux tube crossing. Therefore, we can only estimate the electron energy using Equation 10 (as no radio emission is observed below f_{ce}). Around 02:55:02, Waves measured a radio emission between 1.804 MHz and 1.894 MHz. Based on the Juno/MAG measurements of the magnetic field amplitude, $f_{ce} = 1.7857$ MHz. These values of the emission frequency lead to an estimation of the resonant electron energy in the range [5.1–28.5] keV, and an aperture angle of the beaming cone in the range [70°–81°], provided that Juno actually flew through the radio source. During the crossing, MAG measurements show a ~ 10 nT perturbation in δB_ϕ, while no perturbation is observed in the radial δB_r and compressive $\delta|B|$ components, which indicates again the presence of Alfvénic perturbations and field–aligned currents, with an upward current equatorward of a downward current.

By using UVS, JADE and MAG measurements, Hue et al. (2022) demonstrate that the UV spot connected to the crossed magnetic field lines is fully consistent with a Transhemispheric Electron Beam (TEB), which is reinforced by the $\Delta\lambda_{\text{Alfvén}} = -7°$ calculated using Hue et al. (2023) model. Therefore, we can also conclude that the J–G radio emission source crossed during PJ#30 is associated with a Transhemispheric Electron Beam (TEB) spot uptail of the main Ganymede UV spot.

The results for these two J–G radio source crossings are summarized in Table 1.

4 Summary and Discussion

Concerning the characteristics of the radio emission, the results are similar for the three Galilean moons Io, Europa and Ganymede, in terms of driving mechanism (CMI), electron energy, and beaming. The *in situ* measurements by JADE–E show that the radio emission is triggered by the Cyclotron Maser Instability, driven by a loss–cone electron distribution function. No unstable shell–type electron distribution function are detected in JADE–E measurements. The energy of the resonant electrons is in the range [1–20] keV, and the half–opening cone angle is in the range [74°–86°].

These values are in agreement with those recently obtained using ground–based radio observation, such as the Nançay Decameter Array or NenuFAR, such as the recent work of Lamy et al. (2022) who determined for Io an opening angle $\theta(f)$ in the range [70°–80°] and electron energies in the range [3–16] keV. For Europa, Lamy et al. (2023) mea-

Table 1: Results for the Jupiter–Io, Jupiter–Europa and Jupiter–Ganymede radio emissions source crossings. Is given for each crossing: the name of the moon; the hemisphere of the emission; the associated perijoves; the date and time interval of the radio source crossing as inferred from growth rate calculation when JADE data were available; the JADE data availability; the minimal frequency reached by the radio emission (in MHz); the frequency bandwidth of the emission (in percentage above f_{ce}); the maximum intensity (in $\mathrm{V}^2.\mathrm{m}^{-2}.\mathrm{Hz}^{-1}$) of the emission; the maximum estimated flux (in $\mathrm{W.m}^{-2}.\mathrm{Hz}^{-1}$) of the emission (based on Louis et al., 2021a, 2023); the electron energy (in keV); the opening half–angle of the beaming cone (in °); the radio source size (in km); the downtail distance to the Main Alfvén Wing spot $\Delta\lambda_{\mathrm{Alfvén}}$ (Hue et al., 2023); the associated UV emission at the footprint of the magnetic field line associated to the source (MAW: Main Alfvén Wing: RAW: Reflected Alfvén Wing; TEB: Transhemispheric Electron Beam).

Moon	Io	Io	Io	Io	Europa	Ganymede	Ganymede
Hemisphere	South	North	North	North	North	North	South
Perijove	PJ5	PJ5	PJ6	PJ29	PJ12	PJ20	PJ30
Date (Year–Month–Day)	2017–03–27	2017–03–27	2017–05–19	2020–09–16	2018–04–01	2019–05–29	2020–11–08
Time interval (HH:MM:SS)	09:30:51–59	around 08:34:40	05:39:31–39	02:00:34–36	around 09:15:44	07:37:25–30	around 02:55:02
JADE data	Yes	No	Yes	Yes	No	Yes	No
f_{min} (MHz)	4.7	20.8	12.8	27.7	6.7	6.5	1.8
f_{emission} (% $> f_{ce}$)	$3\text{–}18 \times 10^{-3}$	$3\text{–}29 \times 10^{-3}$	$2\text{–}14 \times 10^{-3}$	$5\text{–}40 \times 10^{-3}$	$7\text{–}15 \times 10^{-3}$	$5\text{–}21 \times 10^{-3}$	$5\text{–}40 \times 10^{-3}$
Intensity max. ($\mathrm{V}^2.\mathrm{m}^{-2}.\mathrm{Hz}^{-1}$)	3×10^{-6}	3×10^{-6}	8×10^{-8}	2×10^{-6}	1×10^{-7}	1×10^{-6}	3.5×10^{-9}
Estimated flux max. ($\mathrm{W.m}^{-2}.\mathrm{Hz}^{-1}$)	4.0×10^{-6}	1.08×10^{-6}	2.5×10^{-7}	7.7×10^{-6}	2.4×10^{-7}	2.4×10^{-6}	7.2×10^{-9}
Electron energy (keV)	1–15	2–20	1–5	3–10	3–8	4–15	2–20
Opening angle	74–85°	74–85°	77–86°	73–84°	79–84°	76–83°	74–85°
Radio source size (km)	360 ± 45	500 ± 100	415 ± 50	250 ± 50	200 ± 49	250 ± 50	75 ± 50
$\Delta\lambda_{\mathrm{Alfvén}}$ (^{o})	3.3^o	10.8^o	87.4^o	7.8^o	-10.5^o	-1.8^o	-7^o
Associated UV emission	RAW	RAW	RAW	RAW	TEB	MAW	TEB

sured on an unique detection an opening angle in the range $\theta = [80°\text{–}86°]$ and an electron energy in the range [0.5–3] keV. For Ganymede, the observations of three emissions lead them to a determination of a beaming angle in the range $\theta = [71°\text{–}87°]$ and an electron energy in the range [0.5–15] keV

The radio sources have a latitudinal extent of a few hundreds of kilometers. In the cases where we are able to constrain the radio source location (provided that we have JADE–E measurement of the up–going electrons), the sources were not crossed anywhere in the flux tube, but only in the downward field–aligned currents.

Based on the previous works of Szalay et al. (2020a, 2020b); Louis et al. (2020); Hue et al. (2022); Rabia et al. (2023) and the recalculated downtail distances from the UV moon main spot using Hue et al. (2023), we also concluded that in the case of Io, all radio source crossed were associated with a RAW UV spot. These crossed radio sources are therefore associated with the secondary radio emissions observed in the usual dynamic spectrum.

In the case of Europa, the only case of radio emission source so far is associated with a TEB spot. Finally, for Ganymede, one radio source is associated with a MAW spot, while the second one is associated with a TEB spot. Even if we didn't detect any radio emission above TEB for Io, these results are in agreement with the interpretation of the first identification of some Io–DAM linked to the TEB spot analyzed in Lamy et al. (2022).

For each source crossed, we estimate the flux density (see Table 1) based on Louis et al. (2021a) and Louis et al. (2023). The maximum values of the estimated flux density in the sources are quite similar between all cases close to the main UV spot, with values in the range $[1\text{–}8]\times10^{-6}$ $\mathrm{W.m}^{-2}.\mathrm{Hz}^{-1}$ in the interval $-1.8^o < \Delta\lambda_{\mathrm{Alfvén}} < 10.8^o$, with a decrease of the intensity with long distance downtail (2.5×10^{-7} $\mathrm{W.m}^{-2}.\mathrm{Hz}^{-1}$ for the case at $\Delta\lambda_{\mathrm{Alfvén}} = 87.4^o$). But with only one case very far downtail, we can't produce a fit of this decrease as a function of $\Delta\lambda_{\mathrm{Alfvén}}$. However, the maximal intensity of the emission is quite smaller for the radio source crossed above a TEB spot (7.2×10^{-9}

and 2.4 × 10^{-7} W.m^{-2}.Hz^{-1}). This could be related to the type of electron distribution, which seems different near tail (non–monotonic) than far tail (broadband), at least for Europa with a separation at $\Delta\lambda_{\text{Alfvén}} \simeq 4^{\circ}$ downtail to the Main spot (Rabia et al., 2023).

From these latest observations, it therefore appears that the cyclotron maser instability driven by a loss–cone electron distribution function is a common way of amplifying radio emission at Jupiter. This is the case both for auroral radio emission (Louarn et al., 2017, 2018) and for moon–induced radio emission (Louis et al., 2020; Hue et al., 2022, and this present study). We have also shown here that the presence of Alfvénic perturbation as well as field–aligned current are necessary for the radio emissions to be amplified. The radio sources are located only in the downward part of the FAC, i.e. when the current is carried by upgoing electrons. This supports the results obtained from very high resolution observations (Zarka et al., 1996; Zarka, 2004; Hess et al., 2007a, 2007b; Louis et al., 2022; Mauduit et al., 2023), which show that the millisecond bursts observed in the J–I and J–G emissions present only negative drifts, i.e. upward–moving electrons. Finally, radio emission are found to be associated with TEB, MAW and RAW spot at the footprint of the flux tube connected to the moons.

However, the Cyclotron Maser Instability does not trigger radio emission at a detectable level for Waves every time Juno is in the flux tube of the moons, even if UV emission is observed at the footprint of the flux tube in each case. Radio sources are crossed in the two cases of Ganymede flux tube crossings. In contrast, a radio source is crossed only once over ten Europa flux tube crossings, while for Io, only four radio sources are crossed over 23 Io flux tube crossings. Therefore, it is clear that several criteria are necessary to amplify a radio wave through the CMI to an observable intensity.

First, we knew that for the CMI to occur, a low energetic plasma is needed ($f_{pe}/f_{ce} \ll 0.1$). But in this study, we also found that the CMI needs to have a sufficiently dense, hot and energetic plasma to occur. If the ratio between f_{pe} and f_{ce} is too low, the integration of the $\delta f/\delta v_{\perp}$ gradient along the resonant circles gives an insufficiently high growth rate to amplify the wave to an observable intensity. For example, in the case where UV emissions are observed at the footprint of the magnetic field lines, the too low electron density in the up-going electron population could be due to an enhanced loss of precipitating electrons in the Jovian ionosphere.

A second necessary condition seems to be the presence of an Alfvénic acceleration process and field–aligned current. As suggested by Crary (1997), accelerated electron beams –up to a few 10s of keV– could be created by repeated Fermi acceleration by field–aligned electric fields produced by the Alfvén waves. If a fraction of this electron population produces UV aurorae at the footprint of the magnetic field lines and another fraction, keeping the $f_{pe}/f_{ce} \ll 0.1$ condition, is accelerated or reflected back upward, this creates a partially empty upward loss cone in the electron distribution function. There are thus $\partial f/\partial v_{\perp}$ gradients within the upward loss cone in the electron distribution function. This therefore creates the instability needed to obtain positive growth rates (see Equation 6), and thus amplify radio emissions via the loss cone–driven CMI.

To resolve the question of the conditions required to amplify a radio wave through the CMI, more crossings of Jupiter-Moon radio emissions will be necessary, and future Juno observations could further illuminate these important processes.

Data Availability Statement

The Juno data used in this manuscript are found at the Planetary Data System at `https://doi.org/10.17189/1522461` for Waves data (Kurth & Piker, 2022), at `https://doi.org/10.17189/1519715` for JADE–E data (Allegrini et al., 2022) and at `https://doi.org/10.17189/1519711` for MAG data (Connerney, 2017).

Acknowledgments

The authors thank the Juno mission team, especially the staff of the Waves, JADE and MAG instruments. C. K. L.'s work at IRAP was supported by CNES. CKL's and CMJ's work at DIAS was supported by Science Foundation Ireland Grant 18/FRL/6199. C. K. L. thanks E. Penou, for the help with the particle analysis through the CLWeb software. V. H. acknowledges support from the French government under the France 2030 investment plan, as part of the Initiative d'Excellence d'Aix–Marseille Université – A*MIDEX AMX–22–CPJ–04. The research at the University of Iowa is supported by NASA through Contract 699041X with the Southwest Research Institute. The research at the Southwest Research Institute is supported by NASA New Frontiers Program for Juno through contract NNM06AA75C. The french authors acknowledge support from CNES and CNRS/INSU national programs of planetology (PNP) and heliophysics (PNST). The authors thank the anonymous referees for their thorough review.

References

Al Saati, S., Clément, N., Louis, C., Blanc, M., Wang, Y., André, N., ... Mauk, B. (2022, October). Magnetosphere-Ionosphere-Thermosphere Coupling Study at Jupiter Based on Juno's First 30 Orbits and Modeling Tools. *Journal of Geophysical Research (Space Physics)*, *127*(10), e2022JA030586. doi: 10.1029/2022JA030586

Allegrini, F., Gladstone, G. R., Hue, V., Clark, G., Szalay, J. R., Kurth, W. S., ... Wilson, R. J. (2020, September). First Report of Electron Measurements During a Europa Footprint Tail Crossing by Juno. *Geophysical Research Letters*, *47*(18), e89732. doi: 10.1029/2020GL089732

Allegrini, F., Wilson, R. J., Ebert, R. W., & Loeffler, C. (2022). *JJUNO J/SW JOVIAN AURORAL DISTRIBUTION CALIBRATED V1.0, JNO-J/SW-JAD-3-CALIBRATED-V1.0 [dataset].* doi: 10.17189/1519715

Bagenal, F., Adriani, A., Allegrini, F., Bolton, S. J., Bonfond, B., Bunce, E. J., ... Zarka, P. (2017, November). Magnetospheric Science Objectives of the Juno Mission. *Space Science Reviews*, *213*, 219-287. doi: 10.1007/s11214-014-0036-8

Bhattacharyya, D., Clarke, J. T., Montgomery, J., Bonfond, B., Gérard, J.-C., & Grodent, D. (2018, January). Evidence for Auroral Emissions From Callisto's Footprint in HST UV Images. *Journal of Geophysical Research (Space Physics)*, *123*, 364-373. doi: 10.1002/2017JA024791

Bigg, E. K. (1964, September). Influence of the Satellite Io on Jupiter's Decametric Emission. *Nature*, *203*, 1008-1010. doi: 10.1038/2031008a0

Bonfond, B., Grodent, D., Badman, S. V., Saur, J., Gérard, J.-C., & Radioti, A. (2017a, August). Similarity of the Jovian satellite footprints: Spots multiplicity and dynamics. *Icarus*, *292*, 208-217. doi: 10.1016/j.icarus.2017.01.009

Bonfond, B., Saur, J., Grodent, D., Badman, S. V., Bisikalo, D., Shematovich, V., ... Radioti, A. (2017b, August). The tails of the satellite auroral footprints at Jupiter. *Journal of Geophysical Research (Space Physics)*, *122*(8), 7985-7996. doi: 10.1002/2017JA024370

Clarke, J. T. (1998). Hubble space telescope imaging of jupiter's uv aurora during the galileo orbiter mission. *Journal of Geophysical Research: Planets*, *103*(E9), 20217-20236. doi: 10.1029/98JE01130

Clarke, J. T., Ajello, J., Ballester, G., Ben Jaffel, L., Connerney, J., Gérard, J.-C., ... Waite, J. H. (2002, February). Ultraviolet emissions from the magnetic footprints of Io, Ganymede and Europa on Jupiter. *Nature*, *415*, 997-1000.

Collet, B., Lamy, L., Louis, C. K., Zarka, P., Prangé, R., Louarn, P., ... Kurth, W. S. (2023). Characterization of Jovian hectometric sources with Juno: statistical position and generation by shell–type electrons. In C. K. Louis, Jackman, C. M., G. Fischer, A. H. Sulaiman, & P. Zucca (Eds.), *Planetary,* *solar and helispheric radio emissions ix.* Trinity College Dublin, Ireland. doi: 10.25546/103095

Connerney, J. E. P. (2017). *Juno MAG CALIBRATED DATA J V1.0, JNO-J-3-FGM-CAL-V1.0 [dataset].* doi: 10.17189/1519711

Connerney, J. E. P., Acuna, M. H., & Ness, N. F. (1981, September). Modeling the Jovian current sheet and inner magnetosphere. *Journal of Geophysics Research*, *86*, 8370-8384. doi: 10.1029/JA086iA10p08370

Connerney, J. E. P., Baron, R., Satoh, T., & Owen, T. (1993, November). Images of Excited H_3ˆ+ at the Foot of the Io Flux Tube in Jupiter's Atmosphere. *Science*, *262*, 1035-1038. doi: 10.1126/science.262.5136.1035

Connerney, J. E. P., Benn, M., Bjarno, J. B., Denver, T., Espley, J., Jorgensen, J. L., … Smith, E. J. (2017, November). The Juno Magnetic Field Investigation. *Space Science Reviews*, *213*, 39-138. doi: 10.1007/s11214-017-0334-z

Connerney, J. E. P., Kotsiaros, S., Oliversen, R. J., Espley, J. R., Joergensen, J. L., Joergensen, P. S., … Levin, S. M. (2018, March). A New Model of Jupiter's Magnetic Field From Juno's First Nine Orbits. *Geophysical Research Letters*, *45*, 2590-2596. doi: 10.1002/2018GL077312

Crary, F. J. (1997, January). On the generation of an electron beam by Io. *Journal of Geophysical Research*, *102*(A1), 37-50. doi: 10.1029/96JA02409

Gershman, D. J., Connerney, J. E. P., Kotsiaros, S., DiBraccio, G. A., Martos, Y. M., -Viñas, A. F., … Bolton, S. J. (2019, July). Alfvénic Fluctuations Associated With Jupiter's Auroral Emissions. *Geophysical Research Letters*, *46*(13), 7157-7165. doi: 10.1029/2019GL082951

Gladstone, G. R., Persyn, S. C., Eterno, J. S., Walther, B. C., Slater, D. C., Davis, M. W., … Denis, F. (2017, November). The Ultraviolet Spectrograph on NASA's Juno Mission. *Space Science Reviews*, *213*, 447-473. doi: 10.1007/s11214-014-0040-z

Goldreich, P., & Lynden-Bell, D. (1969, April). Io, a jovian unipolar inductor. *Astrophysical Journal*, *156*, 59-78. doi: 10.1086/149947

Hess, S. L. G., Cecconi, B., & Zarka, P. (2008, jul). Modeling of Io-Jupiter decameter arcs, emission beaming and energy source. *Geophysical Research Letters*, *35*, L13107. doi: 10.1029/2008GL033656

Hess, S. L. G., Delamere, P., Dols, V., Bonfond, B., & Swift, D. (2010, jun). Power transmission and particle acceleration along the Io flux tube. *Journal of Geophysical Research (Space Physics)*, *115*, A06205. doi: 10.1029/2009JA014928

Hess, S. L. G., Mottez, F., & Zarka, P. (2007b, November). Jovian S burst generation by Alfvén waves. *Journal of Geophysical Research (Space Physics)*, *112*(A11), A11212. doi: 10.1029/2006JA012191

Hess, S. L. G., Zarka, P., & Mottez, F. (2007a, January). Io Jupiter interaction, millisecond bursts and field-aligned potentials. *Planetary Space Science*, *55*(1-2), 89-99. doi: 10.1016/j.pss.2006.05.016

Higgins, C. A. (2007, May). Satellite control of Jovian 2-6 MHz radio emission using Voyager data. *Journal of Geophysical Research (Space Physics)*, *112*, A05213. doi: 10.1029/2006JA012100

Hue, V., Gladstone, G. R., Louis, C. K., Greathouse, T. K., Bonfond, B., Szalay, J. R., … Connerney, J. E. P. (2023, May). The Io, Europa, and Ganymede Auroral Footprints at Jupiter in the Ultraviolet: Positions and Equatorial Lead Angles. *Journal of Geophysical Research (Space Physics)*, *128*(5), e2023JA031363. doi: 10.1029/2023JA031363

Hue, V., Szalay, J. R., Greathouse, T. K., Bonfond, B., Kotsiaros, S., Louis, C. K., … Mauk, B. H. (2022, April). A Comprehensive Set of Juno In Situ and Remote Sensing Observations of the Ganymede Auroral Footprint. *Geophysical Research Letters*, *49*(7), e96994. doi: 10.1029/2021GL096994

Imai, M., Greathouse, T. K., Kurth, W. S., Gladstone, G. R., Louis, C. K., Zarka, P., … Connerney, J. E. P. (2019, Jan). Probing Jovian Broadband Kilometric Radio Sources Tied to the Ultraviolet Main Auroral Oval With Juno. *Geophysical Research Letters*, *46*(2), 571-579. doi: 10.1029/2018GL081227

Imai, M., Kurth, W. S., Hospodarsky, G. B., Bolton, S. J., Connerney, J. E. P., & Levin, S. M. (2017, July). Direction-finding measurements of Jovian low-frequency radio components by Juno near Perijove 1. *Geophysical Research Letters*, *44*, 6508-6516. doi: 10.1002/2017GL072850

Jácome, H. R. P., Marques, M. S., Zarka, P., Echer, E., Lamy, L., & Louis, C. K. (2022, September). Search for Jovian decametric emission induced by Europa on the extensive Nançay Decameter Array catalog. *Astronomy & Astrophysics*, *665*, A67. doi: 10.1051/0004-6361/202244246

Kotsiaros, S., Connerney, J. E. P., Clark, G., Allegrini, F., Gladstone, G. R., Kurth, W. S., ... Levin, S. M. (2019, July). Birkeland currents in Jupiter's magnetosphere observed by the polar-orbiting Juno spacecraft. *Nature Astronomy*, *3*, 904-909. doi: 10.1038/s41550-019-0819-7

Kurth, W. S., Gurnett, D. A., Menietti, J. D., Mutel, R. L., Kivelson, M. G., Bunce, E. J., ... Morooka, M. (2011, January). A Close Encounter with a Saturn Kilometric Radiation Source Region. In H. O. Rucker, W. S. Kurth, P. Louarn, & G. Fischer (Eds.), *Planetary, solar and heliospheric radio emissions (pre vii)* (p. 75-85).

Kurth, W. S., Hospodarsky, G. B., Kirchner, D. L., Mokrzycki, B. T., Averkamp, T. F., Robison, W. T., ... Zarka, P. (2017, November). The Juno Waves Investigation. *Space Science Reviews*, *213*, 347-392. doi: 10.1007/s11214-017-0396-y

Kurth, W. S., & Piker, C. W. (2022). *JUNO E/J/S/SS WAVES CALIBRATED BURST FULL RESOLUTION V2.0, JNO-E/J/SS-WAV-3-CDR-BSTFULL-V2.0 [dataset.* doi: 10.17189/1522461

Lamy, L., Colomban, L., Zarka, P., Prangé, R., Marques, M. S., Louis, C. K., ... Yerin, S. (2022, April). Determining the Beaming of Io Decametric Emissions: A Remote Diagnostic to Probe the Io-Jupiter Interaction. *Journal of Geophysical Research (Space Physics)*, *127*(4), e30160. doi: 10.1029/2021JA030160

Lamy, L., Duchêne, A., Mauduit, E., Zarka, P., Yerin, S., Louis, C., ... Theureau, G. (2023). Probing Jupiter-satellite interactions from the beaming of their decametric emissions: the case of Europa and Ganymede. In C. K. Louis, Jackman, C. M., G. Fischer, A. H. Sulaiman, & P. Zucca (Eds.), *Planetary, solar and heliospheric radio emissions IX.* Trinity Dublin College, Ireland. doi: 10.25546/103097

Lamy, L., Schippers, P., Zarka, P., Cecconi, B., Arridge, C. S., Dougherty, M. K., ... Coates, A. J. (2010, June). Properties of Saturn kilometric radiation measured within its source region. *Geophysical Research Letters*, *37*(12), L12104. doi: 10.1029/2010GL043415

Le Queau, D., Pellat, R., & Roux, A. (1984a, January). Direct generation of the auroral kilometric radiation by the maser synchrotron instability: An analytical approach. *Physics of Fluids*, *27*(1), 247-265. doi: 10.1063/1.864520

Le Queau, D., Pellat, R., & Roux, A. (1984b, May). Direct generation of the auroral kilometric radiation by the maser synchrotron instability: Physical mechanism and parametric study. *Journal of Geophysical Research*, *89*(A5), 2831-2841. doi: 10.1029/JA089iA05p02831

Louarn, P., Allegrini, F., McComas, D. J., Valek, P. W., Kurth, W. S., André, N., ... Zink, J. L. (2017, May). Generation of the Jovian hectometric radiation: First lessons from Juno. *Geophysical Research Letters*, *44*, 4439-4446. doi: 10.1002/2017GL072923

Louarn, P., Allegrini, F., McComas, D. J., Valek, P. W., Kurth, W. S., André, N., ... Wilson, R. J. (2018, September). Observation of Electron Conics by Juno: Implications for Radio Generation and Acceleration Processes. *Geophysical Research Letters*, *45*(18), 9408-9416. doi: 10.1029/2018GL078973

Louis, C. K., Hess, S. L. G., Cecconi, B., Zarka, P., Lamy, L., Aicardi, S., & Loh, A. (2019b, Jul). ExPRES: an Exoplanetary and Planetary Radio Emissions Simulator. *Astronomy & Astrophysics*, *627*, A30. doi: 10.1051/0004-6361/201935161

Louis, C. K., Jackman, C. M., Grießmeier, J. M., Wucknitz, O., McKenna, D. J., Murphy, P. C., ... Vocks, C. (2022, April). Method to observe Jupiter's radio emissions at high resolution using multiple LOFAR stations: a first case study of the Io-decametric emission using the Irish IE613, French FR606, and German DE604 stations. *RAS Techniques and Instruments*, *1*(1), 48-57. doi: 10.1093/rasti/rzac005

Louis, C. K., Lamy, L., Zarka, P., Cecconi, B., & Hess, S. L. G. (2017b, September). Detection of Jupiter decametric emissions controlled by Europa and Ganymede with Voyager/PRA and Cassini/RPWS. *Journal of Geophysical Research (Space Physics)*, *122*, 9228-9247. doi: 10.1002/2016JA023779

Louis, C. K., Lamy, L., Zarka, P., Cecconi, B., Imai, M., Kurth, W. S., ... Levin, S. M. (2017a, September). Io-Jupiter decametric arcs observed by Juno/Waves compared to ExPRES simulations. *Geophysical Research Letters*, *44*, 9225-9232. doi: 10.1002/2017GL073036

Louis, C. K., Louarn, P., Allegrini, F., Kurth, W. S., & Szalay, J. R. (2020, October). Ganymede-Induced Decametric Radio Emission: In Situ Observations and Measurements by Juno. *Geophysical Research Letters*, *47*(20), e90021. doi: 10.1029/2020GL090021

Louis, C. K., Prangé, R., Lamy, L., Zarka, P., Imai, M., Kurth, W. S., & Connerney, J. E. P. (2019a, November). Jovian Auroral Radio Sources Detected In Situ by Juno/Waves: Comparisons With Model Auroral Ovals and Simultaneous HST FUV Images. *Geophysical Research Letters*, *46*(21), 11,606-11,614. doi: 10.1029/2019GL084799

Louis, C. K., Zarka, P., Cecconi, B., & Boudouma, A. (2023). *Juno/Waves estimated flux density Collection (Version 02).* PADC/MASER. doi: 10.25935/fwtq-v202

Louis, C. K., Zarka, P., Dabidin, K., Lampson, P. A., Magalhães, F. P., Boudouma, A., ... Cecconi, B. (2021a, October). Latitudinal Beaming of Jupiter's Radio Emissions From Juno/Waves Flux Density Measurements. *Journal of Geophysical Research (Space Physics)*, *126*(10), e29435. doi: 10.1029/2021JA029435

Mauduit, E., Zarka, P., Lamy, L., & Hess, S. L. G. (2023, October). Drifting discrete Jovian radio bursts reveal acceleration processes related to Ganymede and the main aurora. *Nature Communications*, *14*, 5981. doi: 10.1038/s41467-023-41617-8

McComas, D. J., Alexander, N., Allegrini, F., Bagenal, F., Beebe, C., Clark, G., ... White, D. (2017, November). The Jovian Auroral Distributions Experiment (JADE) on the Juno Mission to Jupiter. *Space Science Reviews*, *213*, 547-643. doi: 10.1007/s11214-013-9990-9

Menietti, J. D., Gurnett, D. A., & Christopher, I. (2001). Control of Jovian radio emission by Callisto. *Geophysical Research Letters*, *28*, 3047-3050. doi: 10.1029/2001GL012965

Mura, A., Adriani, A., Altieri, F., Connerney, J. E. P., Bolton, S. J., Moriconi, M. L., ... Olivieri, A. (2017, June). Infrared observations of Jovian aurora from Juno's first orbits: Main oval and satellite footprints. *Geophysical Research Letters*, *44*(11), 5308-5316. doi: 10.1002/2017GL072954

Mura, A., Adriani, A., Connerney, J. E. P., Bolton, S., Altieri, F., Bagenal, F., ... Turrini, D. (2018, August). Juno observations of spot structures and a split tail in Io-induced aurorae on Jupiter. *Science*, *361*(6404), 774-777. doi: 10.1126/science.aat1450

Mutel, R. L., Menietti, J. D., Gurnett, D. A., Kurth, W., Schippers, P., Lynch, C., ... Cecconi, B. (2010, October). CMI growth rates for Saturnian kilometric radiation. *Geophysical Research Letters*, *37*(19), L19105. doi: 10.1029/2010GL044940

Neubauer, F. M. (1980, March). Nonlinear standing Alfven wave current system at Io - Theory. *Journal of Geophysics Research*, *85*, 1171-1178. doi: 10.1029/JA085iA03p01171

Prangé, R., Rego, D., Southwood, D., Zarka, P., Miller, S., & Ip, W. (1996, January). Rapid energy dissipation and variability of the lo-Jupiter electrodynamic circuit. *Nature*, *379*, 323-325. doi: 10.1038/379323a0

Pritchett, P. L. (1986, December). Cyclotron maser radiation from a source structure localized perpendicular to the ambient magnetic field. *Journal of Geophysical Research*, *91*(A12), 13569-13582. doi: 10.1029/JA091iA12p13569

Rabia, J., Hue, V., Szalay, J. R., André, N., Nénon, Q., Blanc, M., ... Sulaiman, A. H. (2023). Evidence for non-monotonic and broadband electron distributions in the europa footprint tail revealed by juno in situ measurements. *Geophysical Research Letters*, *50*(12), e2023GL103131. Retrieved from `https://agupubs.onlinelibrary.wiley.com/doi/abs/10.1029/2023GL103131` (e2023GL103131 2023GL103131) doi: https://doi.org/10.1029/2023GL103131

Saur, J. (2004, January). A model of Io's local electric field for a combined Alfvénic and unipolar inductor far-field coupling. *Journal of Geophysical Research (Space Physics)*, *109*, A01210. doi: 10.1029/2002JA009354

Szalay, J. R., Allegrini, F., Bagenal, F., Bolton, S. J., Bonfond, B., Clark, G., ... Wilson, R. J. (2020a, February). Alfvénic Acceleration Sustains Ganymede's Footprint Tail Aurora. *Geophysical Research Letters*, *47*(3), e86527. doi: 10.1029/2019GL086527

Szalay, J. R., Allegrini, F., Bagenal, F., Bolton, S. J., Bonfond, B., Clark, G., ... Wilson, R. J. (2020b, September). A New Framework to Explain Changes in Io's Footprint Tail Electron Fluxes. *Geophysical Research Letters*, *47*(18), e89267. doi: 10.1029/2020GL089267

Szalay, J. R., Bonfond, B., Allegrini, F., Bagenal, F., Bolton, S., Clark, G., ... Wilson, R. J. (2018, November). In Situ Observations Connected to the Io Footprint Tail Aurora. *Journal of Geophysical Research (Planets)*, *123*(11), 3061-3077. doi: 10.1029/2018JE005752

Szalay, J. R., Smith, H. T., Zirnstein, E. J., McComas, D. J., Begley, L. J., Bagenal, F., ... Bolton, S. J. (2022, May). Water-Group Pickup Ions From Europa-Genic Neutrals Orbiting Jupiter. *Geophysical Research Letters*, *49*(9), e98111. doi: 10.1029/2022GL098111

Treumann, R. A. (2006, August). The electron-cyclotron maser for astrophysical application. *Astronomy & Astrophysicsr*, *13*, 229-315. doi: 10.1007/s00159-006-0001-y

Wang, Y., Blanc, M., Louis, C., Wang, C., André, N., Adriani, A., ... Tao, C. (2021, September). A Preliminary Study of Magnetosphere-Ionosphere-Thermosphere Coupling at Jupiter: Juno Multi-Instrument Measurements and Modeling Tools. *Journal of Geophysical Research (Space Physics)*, *126*(9), e29469. doi: 10.1029/2021JA029469

Wu, C. S. (1985, August). Kinetic cyclotron and synchrotron maser instabilities - Radio emission processes by direct amplification of radiation. *Space Science Reviews*, *41*, 215-298. doi: 10.1007/BF00190653

Wu, C. S., & Lee, L. C. (1979, June). A theory of the terrestrial kilometric radiation. *Astrophysical Journal*, *230*, 621-626. doi: 10.1086/157120

Zarka, P. (2004, December). Fast radio imaging of Jupiter's magnetosphere at low-frequencies with LOFAR. *Planetary Space Science*, *52*(15), 1455-1467. doi: 10.1016/j.pss.2004.09.017

Zarka, P., Farges, T., Ryabov, B. P., Abada-Simon, M., & Denis, L. (1996, January). A scenario for Jovian S-bursts. *Geophysical Research Letters*, *23*(2), 125-128. doi: 10.1029/95GL03780

Zarka, P., Marques, M. S., Louis, C., Ryabov, V. B., Lamy, L., Echer, E., & Cecconi, B. (2017, January). Radio emission from satellite-Jupiter interactions (especially Ganymede). In G. Fischer, G. Mann, M. Panchenko, & P. Zarka (Eds.), *Planetary radio emissions viii* (p. 45-58). doi: 10.1553/PRE8s45

Zarka, P., Marques, M. S., Louis, C., Ryabov, V. B., Lamy, L., Echer, E., & Cecconi, B. (2018, October). Jupiter radio emission induced by Ganymede and consequences for the radio detection of exoplanets. *Astronomy & Astrophysics*, *618*, A84. doi: 10.1051/0004-6361/201833586